ISSN: 2976-7466

Journal of Biosensors and Bioelectronics Research

Research Article **Open Access**

Metal-ligand Coordination Induced Rapid Li^+ Transport Kinetics through Bidirectional Anchoring Strategy

Jiajun Zhu[1], Ming Zhang[1], Zixuan Fang[1*], Haiping Zhou[1], Jintian Wu[3], Yongqing Yang[1], Zhengwei Li[1], Wenxi Yang[1], Ziqiang Xu[1,2] and Mengqiang Wu[1,2*]

[1]School of Materials and Energy, University of Electronic Science and Technology of China, Chengdu 611731, Sichuan, China

[2]Yangtze Delta Region Institute (HuZhou), University of Electronic Science and Technology of China, Huzhou 313001, Zhejiang, China

[3]School of Chemical Engineering, Sichuan University of Science & Engineering, Zigong 643000, China

ABSTRACT

The unstable interfacial contact and slow Li^+ transport at the side of cathode have been two major challenges for practical application of garnet-based solid-state batteries (SSBs). In this work, a strategy of metal-ligand coordination induced rapid Li^+ transport kinetics through bidirectional anchoring is proposed to address aforementioned issues by decorating the cathode with $Li_{6.4}La_3Zr_{1.4}Ta_{0.6}O_{12}$ (LLZTO) nanoparticles and stabilizing the interface with succinonitrile-based interlayer (SL). The strong metal- ligand coordination of the -CN in SL with the LLZTO solid-state electrolytes and the $LiCoO_2$ (LCO)@LLZTO composite cathode enables an intimate contact at the atomic scale, constructing bidirectional channels of fast Li^+ transport at the interface. Additionally, LLZTO nanoparticles within the composite cathode establish three- dimensional (3D) channels of fast Li^+ transport. The synergistic effect of the bidirectional channels of fast Li^+ transport at the interface and 3D channels of Li^+ transport at internal cathode achieves rapid Li^+ transport kinetics at the cathode side. As a result, a high-capacity retention of 80.6% after 700 cycles at 0.1 C is achieved for the LCO@LLZTO(SL)|LLZTO|Li batteries (3.0-4.2 V, 3 mg·cm-2). It also exhibits excellent cycling performance even at high voltages of 3.0-4.4 V. This work offers a new possibility for fabricating ultra-stable SSBs.

Graphical Abstract

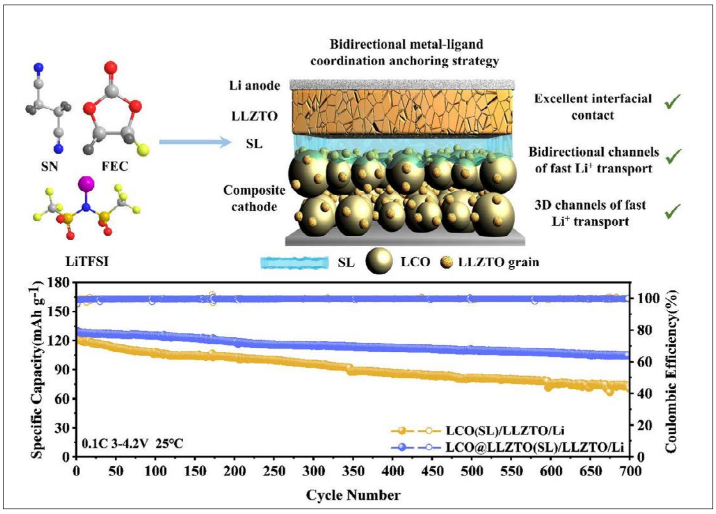

***Corresponding author's**

Mengqiang Wu, School of Materials and Energy, University of Electronic Science and Technology of China, Chengdu 611731, Sichuan, China.

Zixuan Fang, School of Materials and Energy, University of Electronic Science and Technology of China, Chengdu 611731, Sichuan, China.

Received: March 24, 2025; **Accepted:** March 26, 2025; **Published:** April 07, 2025

Keywords: Solid State Batteries, Metal-Ligand Coordination, Anchoring Effect, Composite Cathode, Lithium Metal Batteries

Introduction

To reduce the use of fossil fuels and address the increasingly severe energy crisis, lithium-ion batteries have been widely applied in energy storage devices [1]. Currently, the flammable organic electrolytes used in commercial applications are highly mobile and volatile, making them prone to leakage, combustion, and explosion due to thermal runaway [2]. Moreover, the energy density of liquid lithium-ion batteries has reached its limit. In pursuit of higher energy density, lithium metal, with its high theoretical specific capacity, is considered one of the most promising anode materials [3, 4]. However, the growth of lithium dendrites can cause short circuits, further exacerbating the safety risks associated with liquid lithium metal batteries [5]. Solid-state electrolytes (SSEs), with their flame retardancy and high mechanical strength, can effectively suppress the growth of lithium dendrites and reduce fire hazards, making them the ultimate replacement for liquid electrolytes [6-9].

Among various SSEs, the garnet-type $Li_7La_3Zr_2O_{12}$ (LLZO) stands out as one of the most promising candidates for all-solid-state lithium metal batteries (ASSLMBs) due to its high lithium-ion conductivity and stability against metal anodes [10-13]. However, there is still a significant interfacial resistance between the electrode and the rigid LLZO SSEs, which is due to the inherent poor contact at the electrode/electrolyte interface [14-16]. This issue is particularly severe in the cathode because the volume of active material changes significantly during Li$^+$ intercalation/deintercalation processes, leading to interface delamination, which is detrimental to Li$^+$ transport at the interface [17]. Moreover, LLZO SSEs are completely non-wetting to the cathode, and the limited ion transport performance of the cathode is detrimental to the stability of the battery and the release of capacity [18-20].

To achieve rapid Li$^+$ transport between the composite cathode and SSEs, various strategies have been proposed. For example, Han et al. used a $Li_{2\cdot3}Co_{0\cdot7}B_{0\cdot3}O_3$ sintering aid to co-sinter with composite cathode composed of LCO and LLZO powder, successfully introducing an ion conductor into the cathode and achieving close contact at interface between the composite cathode and garnet SSEs. But composite cathodes prepared by co-sintering method are difficult to achieve high loading mass, and the rigid sintered interface does not support long-term cycling [21]. The addition of interfacial buffer layers, such as liquid electrolytes, ionic liquids, and polymer gels at the interface can reduce interfacial resistance and wet the cathode [15, 22, 23]. However, the liquid electrolytes are continuously consumed during the charging and discharging process. Ionic liquids are prone to decompose at voltages above 4V. Polymer gels have poor compatibility with oxide cathodes and inorganic SSEs, making it struggle to achieve close contact at the interface on an atomic scale. These factors can lead to unstable interface, impeded Li$^+$ transport, and rapid capacity decay in the battery. Compared to these three types of interface layers, plastic crystal succinonitrile (SN) can effectively fill the cathode/garnet interface and has strong oxidative resistance, making it well- suited for high-voltage cathodes [24-26]. At the same time, the nitrile groups (-CN) in SN are commonly used ligands for constructing metal-ligand coordination bonds and have a strong tendency to coordinate with a variety of metal atoms [27, 28]. In previous studies, coordination chemistry has been widely applied in composite solid-state electrolytes, gel electrolytes, and other systems to enhance the mechanical strength of electrolyte matrix, suppress the decomposition of electrolyte, and prevent the side reactions [29, 30]. To date, unfortunately, the significance of strong interaction of coordination to stabilize the interface and accelerate the Li$^+$ transport between cathode and SSEs has been ignored, which inspires us to explore how to fully leverage metal- ligand coordination to maximize its advantages in the ASSLMBs system.

Herein, the strategy of metal-ligand coordination induced bidirectional anchoring is proposed to facilitate fast Li$^+$ transport throughout the side of cathode and construct a stable interface. A SN-based interlayer (SL) containing a large number of -CN is introduced into the interface and able to anchor both of composite cathode and $Li_{6\cdot4}La_3Zr_{1\cdot4}Ta_{0\cdot6}O_{12}$ (LLZTO) SSEs. The La ions exposed on the surface of LLZTO can coordinate with the lone-pair-electrons of the N atoms on -CN. On one hand, the SL can firmly anchor the LLZTO SSEs through metal-ligand coordinate of La ions with -CN. On the other hand, the SL can also anchor the composite cathode, in which LLZTO nanoparticles penetrate deeply into the LCO. The bidirectional anchoring effect induced by metal-ligand coordination between La ions and -CN can achieve an intimate contact at the atomic scale, leading to constructing bidirectional channels of fast Li$^+$ transport at the interface. At the same time, LLZTO nanoparticles in the LCO composite cathode established three dimensional (3D) channels of fast Li$^+$ transport within the cathode. The 3D channels can effectively reduce electrode polarization and improve the release of capacity from LCO active material at internal electrode. The synergistic effect of the bidirectional channels of fast Li$^+$ transport at the interface and 3D channels of Li$^+$ transport within cathode achieves fast Li$^+$ transport kinetics between composite cathode and LLZTO SSEs. The strong coordination between La ions and -CN are systematically studied by comprehensive characterizations and density functional theory (DFT) calculations. The results indicate that LLZTO effectively anchors SN, giving rise to increasing the diffusion of Li$^+$ at the cathode side. Due to the aforementioned beneficial effects, the LCO@LLZTO(SL)|LLZTO|Li batteries can stably work for 700 cycles at 0.1C, with a capacity retention of 80.6%. The metal-ligand coordination induced bidirectional anchoring strategy enhances the compatibility of LLZTO SSEs with high-voltage cathodes, enabling the LCO@LLZTO(SL)|LLZTO|Li batteries to stably cycle for 300 times at 0.1C (3.0-4.4 V, 3 mg·cm-2). This work provides new insights into how to design the long-life and high-voltage ASSLMBs from the perspective of improving the Li$^+$ transport kinetics at cathode side.

Results and Discussion

The Designing Principle of Metal-Ligand Coordination Induced Bidirectional Anchoring Strategy

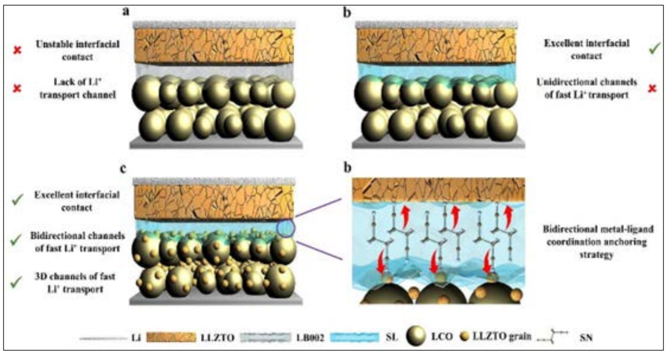

Figure 1: (a) Introducing LE into the Interface between LCO Cathode and LLZTO SSEs. (b) Introducing SL into the Interface between LCO Cathode and LLZTO SSEs. (c) Decorating the Cathode with LLZTO Nanoparticles and Introducing SL into the Interface between LCO@LLZTO Composite Cathode and LLZTO SSEs. (d) Schematic of Metal-Ligand Coordination Induced Bidirectional Anchoring Effect.

Three kinds of models are illustrated in Fig. 1 to compare the origins of resistance to Li$^+$ transport at the side of cathode. Liquid electrolytes are commonly used as interface wetting agents to improve contact between LLZTO and electrodes (Fig. 1a). Due to the volatility and fluidity of liquid electrolytes, the instable interface will be continuously consumed, which leads to a deterioration of kinetics. Substitution of SN- based curing liquid for liquid electrolytes can establish a stable SL between the cathode and LLZTO SSEs (Fig. 1b) [25]. At the same time, the -CN in the SL coordinate with the La ions in LLZTO, achieving an intimate contact at the atomic scale and constructing fast Li$^+$ transport channels between the LLZTO and the SL [31]. However, the contact between the LCO cathode and the SL suffers from interfacial delamination due to interface stress during the electrochemical cycling process. Moreover, Li$^+$ relies entirely on the LCO active material with low ionic conductivity to transport into the interior of cathode, leading to a limited diffusion rate and depth of Li$^+$ [19]. Therefore, LLZTO nanoparticles are employed to decorate the LCO active materials to form LCO@LLZTO composite cathode, which utilizes the metal-ligand coordination between La ions and the -CN in the SL, and significantly enhances the contact between the composite cathode and the SL. This reduces the tensile stress generated at the interface due to volume changes of LCO particles during cycling, effectively preventing interface delamination. The LLZTO nanoparticles at the composite cathode also establish 3D channels for fast Li$^+$ transport [18]. This facilitates the rapid transport of Li$^+$ within the composite cathode, effectively reducing cathode polarization and improving the release of capacity from LCO particles. The strong metal-ligand coordination of -CN with the LLZTO SSEs and the LCO@LLZTO composite cathode allows SL to firmly anchor both the SSEs and composite cathode, constructing bidirectional channels of fast Li$^+$ transport at the interface. As a result, the rapid Li$^+$ transport kinetics within the composite cathode and at the composite cathode/LLZTO interface can be realized through the bidirectional metal-ligand coordination anchoring strategy (synergistic effect of decoration of the LCO@LLZTO composite cathode and the SL) (Fig. 1d).

Analysis of the Metal-Ligand Coordination between LLZTO and SN

First, LLZTO powder is mixed with molten SN. After cooling and standing for two weeks, the chemical stability of LLZTO and SN is studied by X-ray diffraction (XRD). As shown in Fig. 2a, the characteristic peaks of LLZTO match well with the garnet $Li_5L_{a3}Nb_2O_{13}$ structure (JCPDS: 45-0109). The positions of these characteristic peaks do not change after mixing and standing in SN, confirming that LLZTO do not react with SN to form new phases and exhibit good chemical stability. ^{13}C nuclear magnetic resonance (NMR) tests are conducted on pure SN and SN/LLZTO mixtures to study the electronic aggregation state of atoms in SN, as shown in Fig. 2b and c. The ^{13}C nuclear magnetic resonance spectra of pure SN shows a typical peak for methylene (-CH$_2$, orange carbon) carbon at ~13.81 ppm, and the nitrile (-CN, red carbon) carbon has a peak at ~118.60 ppm. By contrast, the resonance of methylene carbon in the mixture of SN/LLZTO shifts to a lower field, and the resonance of nitrile carbon shifts to a higher field. This indicates an increase in electron density around methylene carbon atoms and a decrease in electron density around nitrile carbon atoms. This finding suggests that the interaction between SN and LLZTO leads to a redistribution of electrons in SN [32]. Fig. 2d shows the Raman spectra of LLZTO and SN at different mixing ratios. The -CN of SN corresponds to the peak at 2254cm^{-1}, and as the content of LLZTO increases, the intensity of 2254 cm^{-1} peak decreases, indicating that the interaction between SN and LLZTO is caused by the -CN. X-ray photoelectron spectroscopy (XPS) is further used to study the interaction between SN and LLZTO [33]. As shown in Fig. 2e, compared with the N1s spectra of pure SN, in addition to the -CN peak at 399.85 eV, a strong peak of -CN coordination is observed at 398.58 eV for the SN/LLZTO mixture. This result further indicates that the -CN in SN coordinate with certain metal atoms in LLZTO, leading to an overall decrease in the binding energy of the N1s spectra and an increase in electron density around the N atoms [28,31]. To further investigate the metal atoms coordinated with the -CN, the XPS spectra of La3d in the SN/LLZTO mixture and pure LLZTO are analyzed (Fig. 2f). As for pure LLZTO, two sets of La3d peaks with binding energy of 833.86, 837.97, 850.48, and 854.97 eV can be observed, which shift to higher binding energy of 0.49, 0.39, 0.42, and 0.44 eV after adding SN [34, 35]. At the same time, two new peaks appear at 831.56 eV and 858.20 eV in the La 3d spectra. All of these findings indicate that the -CN of SN coordinate with the La ions in LLZTO. In addition, the increase of binding energy for La3d peak indicates a decrease in electron density around La after coordination with the -CN [36]. The decrease in electron density around La ions and the increase in electron density around N atoms further confirm the coordination between La ions and -CN.

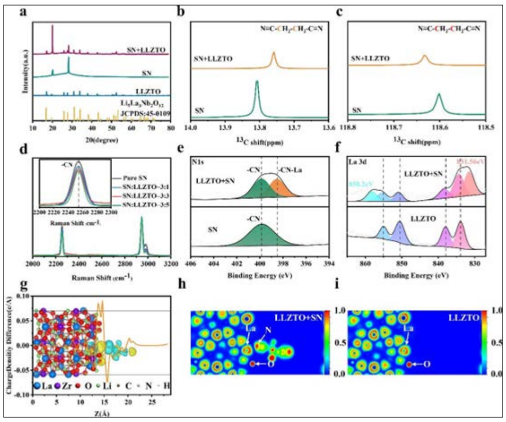

Figure 2: (a) XRD Patterns of LLZTO, SN and SN/LLZTO Mixtures Stored for 2 Weeks. ^{13}C NMR Spectra of (b) Methylene (-CH$_2$, Orange Carbon) Carbon and (c) Nitrile (-CN, Red Carbon) Carbon in Pure SN and SN/LLZTO Mixtures. (d) Raman Shift of Pure SN and SN Mixes with LLZTO of different Mass Ratios. Normalized using the Peak at 2948cm^{-1}. XPS Spectra of (e) N1s and d) La3d of SN and SN/LLZTO Mixtures. (g) The Charge Density difference of SN Adsorbs on LLZO Surface. The Yellow and Blue Regions Represent the Accumulation and Loss of Electrons. (h) ELF Calculations of SN Molecule Adsorbed on LLZO Surface and (i) Pure LLZO Surface

To further elucidate the mechanism of interaction between SN and LLZO, calculations based on density functional theory (DFT) are used to obtain the work function, charge density difference and electron localization function (ELF) of the structural model of SN adsorbed on the LLZO surface (Fig. 2g-i, S1 and S2) [37-39]. The work function of SN is lower than that of LLZO, which means the N atoms in the -CN of SN possess a high electron density and can coordinate with the electron- deficient La ions in LLZO. After SN is adsorbed onto the surface of LLZO, the -CN near the LLZO surface lose electrons along the bond axis, resulting in an increase in potential. However, the differential electron density of SN adsorbed on the LLZO surface indicates that after adsorption, the La ions on the surface of LLZO lose electrons, while the N atoms in -CN gain electrons. This finding is consistent with the chemical shift results of the XPS peaks. This occurs because when -CN comes into contact with LLZO, the N atoms absorb electrons from the surrounding nitrile carbon atoms and transfers them to the outer d-orbit of La ions with which they coordinate [34]. Due to the π-back donation effect, La ions also donate inner orbital electrons to -CN, establishing coordination function [40, 41]. The N atoms absorb electrons from the nitrile carbon and the La ions, increasing the electron density around them. At the same time, the lattice oxygen inside LLZO has a strong electronegativity, causing the electrons in the outer d-orbit of the La ions to transfer towards the nearby lattice oxygen due to its strong ability of electron-withdrawing. This results in a decrease in electron density around the La ions. Moreover, the coordination effect induces the redistribution of electrons in SN, leading to the transfer of electrons around the nitrile carbon and hydrogen atoms to the N atoms and methylene carbon. This finding corresponds to the changes in electron density of carbon atoms in the NMR results. To further confirm the change in electron density of LLZO coordinating with SN, the ELF of SN-adsorbed LLZO model and pure LLZO model are presented in Fig. 2h and i. The results indicate that the electrons around La ions are delocalized, while the electrons around the lattice oxygen are localized, exhibiting a strong electron-binding capability [42]. After -CN coordinates with La ions, the lattice oxygen readily absorbs electrons from the outer d- orbit of La ions. The lattice oxygen absorbs a large number of electrons, giving rise to a decrease in the electron density around La ions.

Beneficial Mechanisms of Metal-Ligand Coordination Induced Bidirectional Anchoring

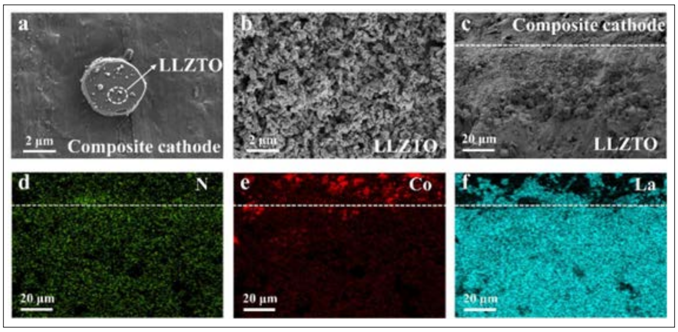

Figure 3: Morphologies of the Composite Cathode, LLZTO Nanoparticles and the Composite Cathode/LLZTO SSEs Interface. SEM Images of (a) the Composite Cathode, (b) the LLZTO Nanoparticles. (c) SEM Cross-Section of the Composite Cathode/ LLZTO SSEs Interface and Corresponding EDS Mapping of (d) N, (e) Co, and (f) La.

The coordination between the -CN and La ions can create a strong connection between the interface layer and the electrolyte, enabling rapid Li⁺ transport between the SL and the LLZTO SSEs. On this basis, we introduce LLZTO nanoparticles into the cathode, aiming to enhance the contact between the SL and the composite cathode through metal-ligand coordination. This approach is intended to address interface delamination caused by volume changes of active materials during long-term cycling [17]. In this work, commercial LCO is used as the cathode active material, and LLZTO nanoparticles decorated LCO are prepared by ball milling and then high-temperature sintering. To obtain the optimal ratio, three decorating ratios of 2 wt.%, 4 wt.%, 8 wt.% are selected to make a comparison [43]. The morphologies of the undecorated LCO and the LCO decorated with LLZTO nanoparticles are shown in Fig. S3, while the electrochemical performances of the LCO/Li batteries are presented in Fig. S4. According to Fig. S3 and S4, the LCO cathode decorated with 4 wt.% LLZTO not only exhibits the most uniform distribution of La and Co but also demonstrates the best cycling stability and rate performance among the three samples. Therefore, the LCO decorated with 4 wt.% LLZTO nanoparticles (LCO@LLZTO) is used as the representative sample to reveal the beneficial effects of the bidirectional metal-ligand coordination anchoring strategy. Scanning electron microscopy (SEM) images of the LCO@LLZTO and LLZTO electrolyte powders are described in Fig. 3a and b, with LLZTO being a few hundred nanometers in size and LCO being a few micrometers in diameter. According to SEM image of LCO@LLZTO, the nanosized LLZTO tightly wraps the surface of the LCO particles. In addition, as shown in Fig. S5, the EDS analysis of the LCO@LLZTO composite cathode also indicates confirms that the Co and La elements are homogeneously distributed, further verifying the uniform distribution of LCO and LLZTO in the composite cathode. Subsequently, the LLZTO SSEs with high ion conductivity are synthesized according to our previous studies (Fig. S6) [44]. The composite cathode is attached to the surface of LLZTO SSEs by using SN-based curing liquid. After cooling down, the SN-based curing liquid is solidified to form an intimate interfacial layer between the composite cathode and the LLZTO SSEs (Fig. 3c). Fig. 3d shows the distribution of N elements at the side of composite cathode, further indicating that the SL effectively fills the gap between the composite cathode and LLZTO SSEs Because LLZTO nanoparticles are introduced into the composite cathode, there are abundant La elements on both sides of the SL layer (Fig. 3e). The - CN can easily coordinate with La ions, which allows the SL to firmly anchor the composite cathode and the LLZTO SSEs, constructing bidirectional channels of fast Li⁺ transport at the interface. As shown in Fig. 3e and f, the EDS spectra of Co and La elements indicate that LLZTO nanoparticles are deeply integrated into the composite cathode, establishing 3D channels of fast Li⁺ transport within the composite cathode. The synergistic effect of nano-decoration of cathode and the SL is going to promote the rapid Li⁺ transport kinetics at the cathode side.

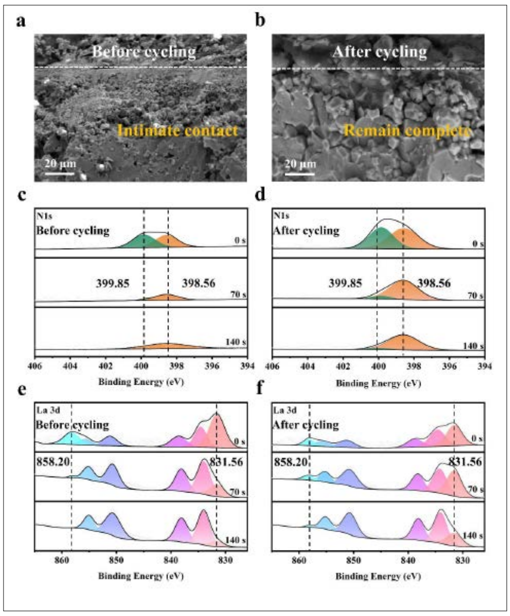

Figure 4: Interfacial Analysis Before and After Cycling. (a, b) SEM Cross-Section of the Composite Cathode/LLZTO SSEs Interface Before and After Cycling. XPS Depth Etching Analysis of the LLZTO SSEs Before and After Cycling. (c, d) N1s and (e, f) La3d.

To explore the influence of electrochemical processes on coordination, SEM and XPS depth etching are used to study the interface modified by bidirectional coordination strategy after 100 cycles. The SEM images show that the interface of composite cathode/LLZTO SSEs remains complete before and after cycling (Fig. 4a and b), with no obvious cracks or pores. This indicates that the SL can effectively reduce cracking caused by interfacial stress, maintaining a stable contact interface between the composite cathode and LLZTO SSEs. To explore why the interface remains stable during cycling, in-depth etching XPS spectra (Fig. 4c-f) are conducted to analyze the effect of cycling process on coordination. As shown in Fig. 4c and d, two peaks located at 399.85 eV and 398.56 eV correspond to the -CN and -CN-La coordination, respectively, and the intensity of both gradually decreases with increasing etching time. After etching for 140 s, the -CN peak disappears and the intensity of the -CN-La coordination peak significantly decreases in the sample before cycling. However, the - CN peak can still be detected in the sample after cycling, with the -CN-La coordination peak exhibiting higher intensity than that of the sample before cycling [27]. Additionally, we compared the nitrogen (N) content on the surface of the samples before and after cycling. At each etching depth, the N content in the sample after cycling is much higher than that in the pre-cycling samples (Fig. S7). This finding indicates that during cycling, due to the intercalation/deintercalation of Li$^+$, the -CN is brought into the interior of the LLZTO SSEs, significantly increasing the number of coordination bonds inside. In addition, the La3d spectra for LLZTO SSEs before and after cycling are shown in Fig. 4e and f. There are four La3d peaks at 833.86, 837.97, 850.48, and 854.97 eV, and it is clear that two extra -CN-La coordination peaks at 831.56 and 858.20 eV can be observed. With an increasing etching time, the intensity of the two coordination peaks gradually decreases. However, at a given etching depth, the coordination peaks of the samples after cycling are significantly larger than those of the samples before cycling. This finding is consistent with the change in the peak of -CN- La coordination in the previous N1s etching spectra, further indicating that the content of -CN-La coordination bonds in the deep layer after cycling is much higher than that before cycling (Fig. S7). As mentioned before, the coordination of -CN with La ions will cause the La3d spectra to shift to a higher binding energy. The binding energies of the La3d spectra peaks of the samples before and after cycling are also compared (Table S1). Under the same etching time, the shift of binding energy of La3d spectra of the sample after cycling is higher than that of the sample before cycling, which also indicates that the sample after cycling has a stronger coordination effect inside. These phenomena indicate that the electrochemical cycling enhances the contact between the SL and the LLZTO SSEs at the atomic scale, leading to an improvement of interfacial compatibility [31]. Therefore, it can effectively inhibit the interfacial delamination during the cycling process. XPS depth etching is also performed on the LCO@LLZTO composite cathode (Fig. S8). Similar to the results of LLZTO SSEs, the content of coordination bonds in the interior of composite cathode after cycling is significantly higher than that before cycling. Therefore, the SL can further strengthen the anchoring effect on the composite cathode and LLZTO SSEs during the cycling process, effectively avoiding interface delamination caused by volume changes of active materials and side reactions during cycling, resulting in stabilizing the channels of bidirectional fast Li$^+$ transport [45, 46].

Excellent Electrochemical Performance of Garnet-Type Solid-State Batteries

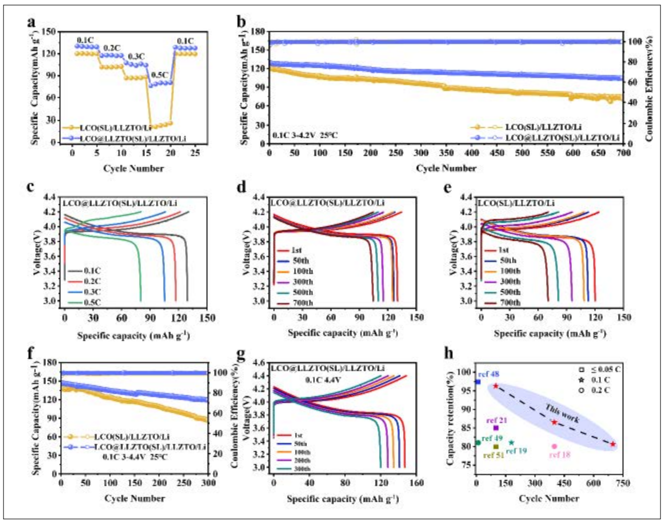

Figure 5: (a) The Rate Performance of LCO@LLZTO(SL)/LLZTO/Li and LCO(SL)/LLZTO/Li Batteries from 0.1 C to 0.5 C. (b) Long-Term Cycling Performance of LCO@LLZTO(SL)/LLZTO/Li and LCO(SL)/LLZTO/Li Batteries at 0.1 C Rate. (c) Charge-Discharge Curves of LCO@LLZTO(SL)/LLZTO/Li Batteries from 0.1 C to 0.5 C. Charge-Discharge curves of (d) LCO@LLZTO(SL)/LLZTO/Li and (e) LCO(SL)/LLZTO/Li Batteries During Cycling at 0.1 C. (f) Long-Term Cycling Performance of LCO@LLZTO(SL)/LLZTO/Li Batteries for High Voltage at 0.1 C rate (3.0-4.4 V). (g) Charge-Discharge Curves of LCO@LLZTO(SL)/LLZTO/Li Batteries During Cycling at 0.1 C(3.0-4.4V). (h) Comparison of Electrochemical Performance with Existing Literature.

The performances of full batteries further demonstrate the beneficial effects of the metal-ligand coordination induced bidirectional anchoring strategy on practical applications. The electrochemical performance of LCO|LLZTO|Li batteries at different rates from 0.1 C to 0.5 C at 3.0-4.2 V is shown in Fig. 5a, c and S9. The rate performance of the LCO@LLZTO(SL)|LZZTO|Li batteries which employs the metal-ligand coordination induced bidirectional anchoring strategy is significantly better than that of the LCO(SL)|LLZTO|Li batteries. This result indicates that the decoration of LLZTO particles on LCO accelerates the transfer of Li$^+$ inside the cathode, and the LCO@LLZTO composite cathode has higher ionic conductivity, which is beneficial for the release of capacity [18,19]. The capacity of LCO(LE)|LLZTO|Li using LE as the interfacial layer exhibits significant capacity decay and poor reversibility when the rate returns to 0.1 C although it presents similar rate performance to that of the LCO@LLZTO(SL)|LLZTO|Li batteries. This result is highly related to the continuous consumption of the LE during cycling.

Fig. 5b shows the long-term cycling performance of the batteries at 0.1C from 3.0 - 4.2 V. The initial discharge capacity of the LCO@LLZTO(SL)|LLZTO|Li batteries are 129.9 mAh g^{-1}, with a capacity retention of 86.5% after 400 cycles. Even after 700 cycles, the capacity retention remains at 80.6%, indicating excellent cycling stability. By contrast, the initial discharge capacity of the LCO(SL)|LLZTO|Li batteries are only 120 mAh g^{-1}, with a capacity retention of 61.7% after 700 cycles. This is attributed to the absence of 3D channels for fast Li$^+$ transport within the bare LCO cathode, which affects the release of capacity. During long-term cycling, volume changes of the cathode active material cause delamination between the composite cathode and the SL, disrupting the Li^+ transport channels at the interface and leading to continuous capacity decay. At the same time, a long-cycling test is also performed on the batteries with the LCO cathode interfaced with liquid electrolytes, but the capacity retention is only 31.6% after 200 cycles, which is much worse than the SL with coordination with La ions (Fig. S10). In addition, the LCO@LLZTO(SL)|LLZTO|Li batteries also exhibit excellent long-cycle performance at 0.5C, with a capacity retention of 97.6% after 500 cycles (Fig. S11). Fig. 5d and 5e show the charge-discharge curves of the batteries using LCO@LLZTO and LCO cathodes, respectively. The initial polarization voltage of the SSBs using the LCO@LLZTO composite cathode is significantly lower than that of the batteries using the LCO cathode, showing a very low value of 0.08 V. The addition of LLZTO ion conductor within the cathode constructs fast Li^+ transport paths. Meanwhile, bidirectional channels of fast Li^+ transport at the interface are built through the metal- ligand coordination between La ions and -CN, enabled by the bidirectional anchoring effect. This facilitates rapid transport of Li^+ throughout the cathode side. Even after 700 cycles, the polarization voltage does not increase significantly. By contrast, the polarization of the batteries using the LCO cathode rises sharply after 100 cycles, but it is better than that of LCO(LE)|LLZTO|Li (Fig. S10).

To verify the stability of the SL at high voltage, the LCO@ LLZTO(SL)|LLZTO|Li and LCO(SL)|LLZTO|Li batteries are assembled and cycled at 0.1 C from 3.0-4.4 V, as shown in Fig. 5f and g. The initial capacity of the LCO@LLZTO(SL)|LLZTO|Li is 147.3 mAh g^{-1}, with a capacity retention of 81.6% after 300 cycles. In contrast, the LCO(SL)|LLZTO|Li batteries have a lower initial capacity and poorer capacity retention. Even at the higher rate of 0.5 C, the LCO@LLZTO(SL)|LLZTO|Li batteries still have a capacity retention of 90.6% after 500 cycles, demonstrating excellent high-voltage cycling stability (Fig. S12). These electrochemical results indicate that the metal-ligand coordination induced bidirectional anchoring strategy has achieved rapid Li^+ transport kinetics between the composite cathode and LLZTO SSEs, and greatly improves the discharge capacity and cycling stability of the batteries. As shown in Fig. 5h and Table S2, our work has a significant advantage in terms of battery cycling capacity and stability over the latest literatures, indicating that the metal-ligand coordination induced bidirectional anchoring strategy is very effective to promote kinetics in SSBs [18, 19, 21, 47-51].

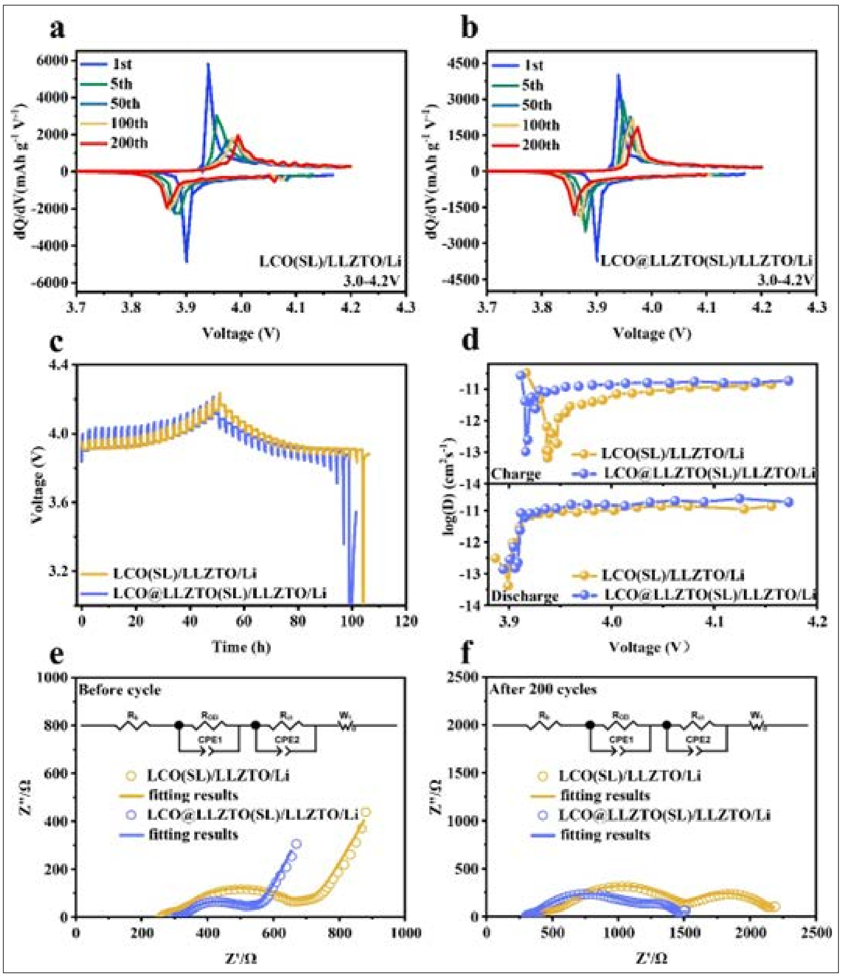

Figure 6: The Corresponding dQ/dV Curves of (a) LCO/LLZTO/Li and (b) LCO@LLZTO(SL)/LLZTO/Li Batteries at Selected Cycles for Long-Term Cycling. (c)The GITT Curves and (d) the Li^+ Diffusion Coefficients of LCO/LLZTO/Li and LCO@LLZTO(SL)/LLZTO/Li Batteries During the 1st Charge-Discharge Process. The EIS of LCO/LLZTO/Li and LCO@LLZTO(SL)/LLZTO/Li Batteries (e) before and (f) after 200 Cycles (Insets are the Equivalent Circuit used to fit the EIS Curves).

To study the polarization of different composite cathodes during cycling, we conduct dQ/dV tests and evaluate the electrode polarization based on the difference between the oxidation peak position and the reduction peak position (dV). As shown in Fig. 6a and b, the dV values of the LCO cathode and LCO@LLZTO cathode are nearly identical during the first cycle, both measuring 0.04 V. After 200 cycles, the oxidation peak of the LCO cathode shifts significantly to the positive direction, and its dV value increases to 0.136V. This indicates a rapid increase in electrode polarization Additionally, the intensity of the oxidation peak decreases significantly, indicating irreversible destruction of the crystal structure during cycling. In contrast, the LCO@LLZTO cathode exhibits more reversible oxidation and reduction peaks, with minimal change in dV and intensity. This is attributed to the incorporation of the LLZTO ion conductor, which accelerates the transfer of Li^+ between particles within the cathode. This effectively reduces the polarization of the electrode, mitigates the structural collapse of the cathode surface caused by over- deintercalation of Li^+, and maintains the stability of the electrode structure [52].

In addition, galvanostatic intermittent titration technique (GITT) tests are conducted to explore the effect of modification on Li^+ diffusion kinetics, and the lithium-ion diffusion coefficient (D_{Li^+}) is calculated according to the GITT results and Fick's second law. As shown in Fig. 6c and d, the LCO@LLZTO(SL)|LLZTO|Li batteries have lower electrochemical polarization and stronger reversibility during charge- discharge. At the same time, the D_{Li^+} calculated according to GITT shows that the LCO@LLZTO(SL)|LLZTO|Li batteries have higher D_{Li^+} compared to the LCO(SL)|LLZTO|Li batteries. This enhancement in D_{Li^+} is due to the metal-ligand coordination constructing fast Li^+ transport channels between the composite cathode and the SL. Moreover, the LLZTO nanoparticle decorating layer has excellent Li^+ conductivity. The synergistic effect of these two factors ensures faster Li^+ transport kinetics of the batteries during charge-discharge.

To further understand the changes in interfacial resistance, the electrochemical impedance spectroscopy (EIS) of the batteries before and after cycling is studied, and the Nyquist diagrams with corresponding equivalent circuits are shown in Fig. 6e, f and S10. Before cycling, the incomplete semicircle (R_b) at high frequency represents the total resistance of the solid electrolyte and SL. The first semicircle (R_{ct}) at medium frequency represents the interfacial resistance, and the straight line (W1) at low frequency is related to Li^+ diffusion resistance. After 200 cycles, a new semicircle (R_{cei}) appears in the medium frequency region of the batteries with the SL. This semicircle is attributed to the formation of a CEI film during cycling, with LiF being the main component (Fig. S8) [53]. The continuous thickening of the LiF layer with the increase of cycle time is the primary reason for the observed increase in impedance during cycling. By comparing the EIS fitting results of LCO(SL)|LZZTO|Li and LCO@LLZTO(SL)|LZZTO|Li batteries before and after cycling, it can be found that the LCO@LLZTO(SL)|LZZTO|Li batteries have a lower Rct before cycling. After 200 cycles, the Rct of the LCO@LLZTO(SL)|LLZTO|Li batteries only increase by about 100 Ω, while the Rct value of the pure LCO cathode batteries almost doubles. This indicates that the atomic-level interactions produced at the interface by the metal-ligand coordination induced bidirectional anchoring strategy can effectively avoid interface cracking caused by volume changes of the cathode active material during cycling, thereby reducing interfacial resistance.

Conclusion

In this study, a bidirectional metal-ligand coordination anchoring strategy is implemented by decorating the cathode with LLZTO nanoparticles and introducing SL into the interface between the composite cathode and SSEs. The SL can coordinate with La ions from the LLZTO nanoparticles in the composite cathode and the surface of LLZTO SSEs, which is beneficial for interfacial stability and constructs bidirectional channels of fast Li^+ transport, accelerating Li^+ transport at the interface. The LLZTO nanoparticles establish 3D channels of fast Li^+ transport within the composite cathode, enhancing its ionic conductivity. The synergistic effect of the bidirectional channels of fast Li^+ transport at the interface and 3D channels of fast Li^+ transport in the cathode achieves rapid Li^+ transport kinetics on the cathode side of garnet-based all-solid-state batteries. As a result, the LCO@LLZTO(SL)|LLZTO|Li batteries exhibit a high discharge specific capacity and excellent cycling stability. The batteries have an initial discharge specific capacity of 129.9 mAh g^{-1} at 0.1 C, with a capacity retention of 86.5% after 400 cycles. Even after 700 cycles, the capacity retention remains at 80.6%. The LCO@LLZTO(SL)|LLZTO|Li batteries at 3.0-4.4 V can also achieve a stable cycling for over 300 cycles at 0.1 C. This work further elucidates the role mechanism of coordination chemistry in the cathode interface of SSBs, providing a promising pathway for the practical application of ASSLMBs.

Acknowledgment

We greatly acknowledge the financial support from Natural Science Foundation of Sichuan Province (Grant No. 2025ZNSFSC0100).

Highlights

- Interfacial metal-ligand coordination firmly anchors composite cathode and SSEs.
- 3D channels of fast Li^+ transport at internal composite cathode are constructed.
- Bidirectional channels of fast Li^+ transport at the interface are constructed.
- The fast Li^+ transport kinetics achieves excellent capacity and cycling stability.

Declaration of interests

☒The authors declare that they have no known competing financial interests or personal relationships that could have appeared to influence the work reported in this paper.

☐The authors declare the following financial interests/personal relationships which may be considered as potential competing interests.

References

1. M Li, J Lu, Z Chen, K (2018) Amine, 30 Years of Lithium-Ion Batteries. Adv Mater 30.
2. K Xu (2014) Electrolytes and Interphases in Li-Ion Batteries and Beyond. Chem Rev 114: 11503-11618.
3. M Winter, B Barnett, K Xu (2018) Before Li Ion Batteries. Chem Rev 118: 11433-11456.
4. M Armand, JM Tarascon (2008) Building better batteries. Nature 451: 652-657.
5. A Jana, SI Woo, KSN Vikrant, RE García (2019) Electrochemomechanics of lithium dendrite growth. Energy & Environ Sci 12: 3595-3607.
6. X Zhang, S Wang, C Xue, C Xin, Y Lin, Y Shen, et al. () Self-Suppression of Lithium Dendrite in All-Solid-State Lithium Metal Batteries with Poly (vinylidene difluoride)-Based Solid Electrolytes. Adv Mater 31: 1806082.

7. J Janek, WG Zeier (2016) A solid future for battery development. Nat Energy 1: 16141.
8. JC Bachman, S Muy, A Grimaud, HH Chang, N Pour, et al. (2016) Inorganic Solid-State Electrolytes for Lithium Batteries: Mechanisms and Properties Governing Ion Conduction. Chem Rev 116: 140-162.
9. J Chen, J Wu, X Wang, AA Zhou, Z Yang (2021) Research progress and application prospect of solid-state electrolytes in commercial lithium-ion power batteries. Energy Storage Mater 35: 70-87.
10. R Murugan, V Thangadurai, W Weppner (2007) Fast Lithium-Ion Conduction in Garnet-Type Li7La3Zr2O12. Angew Chem Int Ed 46: 7778-7781.
11. GV Alexander, C Shi, J O'Neill, ED Wachsman (2023) Extreme lithium-metal cycling enabled by a mixed ion- and electron-conducting garnet three-dimensional architecture. Nature Materials 22: 1136-1143.
12. S Han, Z Wang, Y Ma, Y Miao, X Wang, et al. (2023) Fast ion-conducting high-entropy garnet solid-state electrolytes with excellent air stability. Journal of Advanced Ceramics 12: 1201-1213.
13. X Xiang, Z Fang, C Du, Z Zhao, J Chen, et al. (2024) Constructing electron-blocking grain boundaries in garnet to suppress lithium dendrite growth. Journal of Advanced Ceramics 13: 166-175.
14. X Ji, Y Zhang, M Cao, Q Gu, H Wang, et al. (2022) Advanced inorganic/polymer hybrid electrolytes for all-solid-state lithium batteries. Journal of Advanced Ceramics 11: 835-861.
15. X Wang, Y Wang, Y Wu, Y Fan, Y Tian (2023) Dual-interlayers constructed by Ti3C2Tx/ionic-liquid for enhanced performance of solid garnet batteries. J Energy Chem 78: 47-55.
16. J Wu, Z You, M Li, H Chen, S Feng, et al. (2024) Synergistic Reduction and Oxidation Resistant Interface Modifier for High-Voltage and High-Loading Solid-State Lithium Batteries. Adv Energy Mater 15.
17. AY Hou, CY Huang, CL Tsai, CW Huang, R Schierholz, et al. (2022) All-Solid-State Garnet-Based Lithium Batteries at Work–In Operando TEM Investigations of Delithiation/Lithiation Process and Capacity Degradation Mechanism. Advanced Science 10.
18. Z Bi, N Zhao, L Ma, Z Fu, F Xu, et al. (2020) Interface engineering on cathode side for solid garnet batteries. Chemical Engineering Journal 387.
19. YN Yang, YX Li, YQ Li, T Zhang (2020) On-surface lithium donor reaction enables decarbonated lithium garnets and compatible interfaces within cathodes. Nature Communications 11.
20. X Han, S Wang, Y Xu, G Zhong, Y Zhou, et al. (2021) All solid thick oxide cathodes based on low temperature sintering for high energy solid batteries. Energy & Environ Sci 14: 5044-5056.
21. F Han, J Yue, C Chen, N Zhao, X Fan, et al. (2018) Interphase Engineering Enabled All-Ceramic Lithium Battery. Joule 2: 497-508.
22. X Han, Y Gong, K Fu, X He, GT Hitz, et al. (2016) Negating interfacial impedance in garnet-based solid-state Li metal batteries. Nature Materials 16: 572-579.
23. L Nie, S Chen, M Zhang, T Gao, Y Zhang, et al. (2023) An in-situ polymerized interphase engineering for high-voltage all-solid-state lithium-metal batteries. Nano Research 17: 2687-2692.
24. R Chen, F Liu, Y Chen, Y Ye, Y Huang, et al. (2016) An investigation of functionalized electrolyte using succinonitrile additive for high voltage lithium-ion batteries. J Power Sources 306: 70-77.
25. Z Lu, J Yu, J Wu, MB Effat, SCT Kwok, et al. (2019) Enabling room-temperature solid-state lithium-metal batteries with fluoroethylene carbonate-modified plastic crystal interlayers. Energy Storage Mater 18: 311-319.
26. Z Zhang, M Zhang, J Wu, X Hu, B Fu, et al. (2023) Interfacial Plasticization Strategy Enabling a Long-Cycle-Life Solid-State Lithium Metal Battery. Small 20.
27. Y Ji, Z Zhang, M Gao, Y Li, MJ McDonald, et al. (2015) Electrochemical Behavior of Suberonitrile as a High-Potential Electrolyte Additive and Co-Solvent for Li [Li0.2Mn0.56Ni0.16Co0.08] O2 Cathode Material. J Electrochem Soc 162: A774-A780.
28. J Zhao, Y Liang, X Zhang, Z Zhang, E Wang, et al. (2020) In Situ Construction of Uniform and Robust Cathode–Electrolyte Interphase for Li-Rich Layered Oxides. Adv Funct Mater 31.
29. Q Wang, H Xu, Y Fan, SS Chi, B Han, et al. (2024) Insight into Multiple Intermolecular Coordination of Composite Solid Electrolytes via Cryo-Electron Microscopy for High-Voltage All- Solid-State Lithium Metal Batteries. Adv Mater 36.
30. J Wu, L Huang, S Wang, X Li, L Wen, et al. (2023) Ionogel electrolyte with dynamic metal-ligand interactions enabled self-healable supercapacitor with high energy density. Energy Storage Mater 57: 549-556.
31. G Yang, X Bai, Y Zhang, Z Guo, C Zhao, et al. (2022) A Bridge between Ceramics Electrolyte and Interface Layer to Fast Li^+ Transfer for Low Interface Impedance Solid-State Batteries. Adv Funct Mater 33.
32. F Fu, Y Liu, C Sun, L Cong, Y Liu, et al. (2022) Unveiling and Alleviating Chemical "Crosstalk" of Succinonitrile Molecules in Hierarchical Electrolyte for High-Voltage Solid-State Lithium Metal Batteries. Energy & Environ. Mater 6.
33. X Zhang, T Liu, S Zhang, X Huang, B Xu, et al. (2017) Synergistic Coupling between Li6.75La3Zr1.75Ta0.25O12 and Poly (vinylidene fluoride) Induces High Ionic Conductivity, Mechanical Strength, and Thermal Stability of Solid Composite Electrolytes. Journal of the American Chemical Society 139: 13779-13785.
34. YN Yang, FL Jiang, YQ Li, ZX Wang, T Zhang (2021) A Surface Coordination Interphase Stabilizes a Solid-State Battery. Angew Chem Int Ed 60: 24162- 24170.
35. WS Scheld, K Kim, C Schwab, AC Moy, SK Jiang, (2023) The Riddle of Dark LLZO: Cobalt Diffusion in Garnet Separators of Solid-State Lithium Batteries. Adv Funct Mater 33.
36. Y Shang, X Xu, B Gao, Q Yue (2018) Highly selective and efficient removal of fluoride from aqueous solution by Zr La dual-metal hydroxide anchored bio-sorbents. Journal of Cleaner Production 199: 36-46.
37. T Lu, F Chen (2011) Multiwfn: A multifunctional wavefunction analyzer, Journal of Computational Chemistry 33: 580-592.
38. T Lu, F Chen (2012) Quantitative analysis of molecular surface based on improved Marching Tetrahedra algorithm. Journal of Molecular Graphics and Modelling 38: 314-323.
39. J Zhang, T Lu (2021) Efficient evaluation of electrostatic potential with computerized optimized code. Physical Chemistry Chemical Physics 23: 20323-20328.
40. ML Kuznetsov, EA Klestova Nadeeva, AI Dement'ev (2004) Theoretical study on reactivity of coordinated nitriles: structure, bonding and reactivity of [ReCl4(N CCH3)2]. Journal of Molecular Structure: THEOCHEM 671: 229-237.
41. C Tian, E Kan, C Lee, MH Whangbo (2010) π-Back-Donation Effect of the Cyanide Ligands on the Electron Correlation and Charge Transfer in Prussian Blue RbMn [Fe (CN) 6].

Inorganic Chemistry 49: 3086-3088.

42. S Gao, Z Zhu, H Fang, K Feng, J Zhong, et al. (2024) Regulation of Coordination Chemistry for Ultrastable Layered Oxide Cathode Materials of Sodium-Ion Batteries. Adv Mater 36.
43. X Wang, H Ren, Y Du, Z Li, W Zhao, et al. (2024) Tuning surface chemistry to reduce the step-like degradation of LiCoO2 at 4.6 V. Nano Energy 125.
44. Z Xu, X Hu, B Fu, K Khan, J Wu, et al. (2023) Co-doping strategy enhanced the ionic conductivity and excellent lithium stability of garnet-type Li7La3Zr2O12 electrolyte in all solid-state lithium batteries. J Materiomics 9: 651-660.
45. H Huo, J Luo, V Thangadurai, X Guo, CW Nan, et al. (2019) Li2CO3: A Critical Issue for Developing Solid Garnet Batteries. ACS Energy Lett 5: 252-262.
46. B Liao, X Hu, M Xu, H Li, L Yu, et al. (2018) Constructing Unique Cathode Interface by Manipulating Functional Groups of Electrolyte Additive for Graphite/LiNi0.6Co0.2Mn0.2O2 Cells at High Voltage. The Journal of Physical Chemistry Letters 9: 3434-3445.
47. V Kiyek, C Schwab, WS Scheld, C Roitzheim, A Lindner, et al. (2024) Direct Precursor Route for the Fabrication of LLZO Composite Cathodes for Solid-State Batteries. Advanced Science 11.
48. KJ Kim, JLM Rupp (2020) All ceramic cathode composite design and manufacturing towards low interfacial resistance for garnet-based solid-state lithium batteries. Energy & Environ Sci 13: 4930-4945.
49. K Park, BC Yu, JW Jung, Y Li, W Zhou, et al. (2016) Electrochemical Nature of the Cathode Interface for a Solid-State Lithium-Ion Battery: Interface between LiCoO2 and Garnet-Li7La3Zr2O12. Chemistry of Materials 28: 8051-8059.
50. S Ohta, J Seki, Y Yagi, Y Kihira, T Tani, et al. (2014) Co-sinterable lithium garnet-type oxide electrolyte with cathode for all-solid-state lithium-ion battery. J Power Sources 265: 40-44.
51. EJ Cheng, M Shoji, T Abe, K Kanamura (2022) Ionic liquid-containing cathodes empowering ceramic solid electrolytes. iScience 25.
52. R He, G Tian, S Li, Z Han, W Zhong, et al. (2022) Enhancing the Reversibility of Lithium Cobalt Oxide Phase Transition in Thick Electrode via Low Tortuosity Design. Nano Lett 22: 2429-2436.
53. A Fu, Z Zhang, J Lin, Y Zou, C Qin, et al. (2022) Highly stable operation of LiCoO2 at cut-off ≥ 4.6 V enabled by synergistic structural and interfacial manipulation. Energy Storage Mater 46: 406-416.